



# Study on the mechanical behavior of sands using 3D discrete element method with realistic particle models

Wen-Jie Xu<sup>1</sup> · Guang-Yu Liu<sup>1</sup> · Han Yang<sup>2</sup>

Received: 31 October 2018 / Accepted: 3 May 2020 / Published online: 21 May 2020  
© Springer-Verlag GmbH Germany, part of Springer Nature 2020

## Abstract

Presented is a study on the geometrical characteristics of sand particles and the mechanical behavior of sand material under external loading. Based on computed tomography technique, a reconstruction method of granular particles was developed and used to build a database of 3D geometrical models for sand particles. The studied sand particles showed good regularities in morphological characteristics and thus were suitable to be used for the random generation of numerical samples. DEM tests using realistically shaped particles were proven to better simulate the mechanical behavior of the sample during elastoplastic loading stage, which was an issue for the simplified spherical particles. The generation, extension, and breakage of the force chains controlled the strain softening behavior of sands. Anisotropy analysis using the spherical harmonic series showed that the evolution of anisotropy directions and parameters corresponded well with the macroscopic mechanical behavior of the material. Pore volume computation based on Voronoi diagram was performed to illustrate the formation and evolution of localized shear zone. The mesoscopic analysis showed that particle shape significantly influences the mechanical behavior of sands and thus should be properly modeled in numerical simulations.

**Keywords** 3D particle · Direct shear test · Discrete element method (DEM) · Failure mechanism · Granular material

## 1 Introduction

As a common granular material in geotechnical engineering, many numerical and experimental investigations on sands have been conducted in the recent few decades. The multi-scale mechanical behavior of sands has proven to be a key factor in engineering designs of embankments, foundations, slopes, and other infrastructures. Many numerical methods have been developed and used to simulate granular materials, like sands, on constitutive level and in practical engineering problems. More and more researchers noticed that the geometric shape performed important influence on the mechanical behaviors of granular materials [34, 37]. Previously, the researchers were

mainly focused on the 2D model of the particles based on 2D images [11]. In the past decades, with the development of the techniques, the 3D surface of the particles can easily be obtained by laser scanning [19] or computed tomography [10]. At the same time, a series of methods have been developed to construct the 3D model of the particles, such as Fourier series 3D expansion method [22], machine learning [18], and spherical harmonic function method [7].

Due to its capability of simulating the behavior of each particle, discrete element method (DEM) has proven to be effective in the modeling of sands. Using DEM simulations, the anisotropic fabric evolution and localization phenomenon in granular materials on meso- and macro-scales were studied in several papers [9, 16, 17, 30, 39]. As shown in the studies by Santamarina and Cho [29] and Salazar et al. [28], particle shape has a significant influence on the physical and mechanical behaviors of granular materials. It has been shown that DEM simulations using spherical particles tend to underestimate the friction angle and shear strength of granular materials [27, 29]. To reduce this kind of influence, Iwashita and Oda [12] presented a rolling resistance method that can account for the moments

✉ Wen-Jie Xu  
wenjiexu@tsinghua.edu.cn

<sup>1</sup> State Key Laboratory of Hydrosience and Hydraulic Engineering, Department of Hydraulic Engineering, Tsinghua University, Beijing 100084, China

<sup>2</sup> Department of Civil and Environmental Engineering, University of California, Davis, CA 95616, USA

between particles which are transferred through contacts and resisted particle rotations. And recently, Zhao et al. [41] have addressed some deficiencies of using the rolling resistance model. Many researchers have worked on the DEM analysis based on sophisticated particle shapes, such as 3D oval particles [20, 24], overlapping rigid clusters [19], convex polyhedral [8], superellipsoid [41], and level set [26]. As we know, the contact detection algorithm for spheres is easier than other types of particles. And, generally, the sphere clumping approach has advantage in computational efficiency. Furthermore, it can easily be used for sophisticated particle shape [19]. So, the overlapping rigid clusters approach proposed by Li et al. [19], which can finely represent a sophisticated particle with few spheres, is adopted in this study.

Direct shear test is one of the most commonly used testing methods for determining shear strength of geotechnical materials [13, 23, 35]. To gain insight on the meso-structure evolution of sand samples under shear loading, numerical simulations of direct shear tests using DEM have been conducted. In earlier studies that use DEM to simulate direct shear test, the evolution of shear band and its relationship with the macro-behavior of sand samples were discussed [3, 6, 32, 40]. However, most studies focused on 2D problems, and the shapes of particles were simplified to be circular or spherical. This largely ignores the important influence of the angularity of large particles on the mechanical behavior of granular materials. In this paper, it is shown that the mechanical behavior of sands can be better represented in DEM simulations if modeled with realistically shaped particles.

Deformation localization is a common phenomenon observed in granular materials under external loads. Dilatation, occlusion, particle rotation, anisotropy, and other meso-structural characteristics are fundamental physical processes found in the localization zone. To quantify the localization behavior in geotechnical material, digital image correlation [25], ultrasonic tomography, X-ray tomography, 3D volumetric digital image correlation [5], and other nondestructive methods have been used in earlier studies. However, the reliability of certain methods may be affected for various reasons, and some experiments are very expensive. On the other hand, DEM simulations are much cheaper and repeatable, while the reliability of the results can be easily verified through simple laboratory tests.

Presented in this study is a numerical system that can simulate the mechanical behavior of sands with realistically shaped particles using 3D discrete element method. As the first step, the 3D shape information of sand particles has been obtained using computed tomography (CT) and stored in a database. Using this database, the DEM model of the sand sample used in this study was generated. The

properties of contacts between sand particles are determined by calibrating numerical results with the laboratory test results. A series of simulations of the sand sample under different loading conditions were performed. And various aspects of the mechanical behavior of sand on meso- and macro-scale were discussed.

## 2 3D geometric modeling of sand particles

The sand sample used in this study was taken from Fujian, China (Chinese standard method, GB/T17671-1999). The sample was sieved through round-hole sieves so that the sand particles with diameters between 1.0 and 2.0 mm can be picked out for further use (Fig. 1a).

### 2.1 CT scan and reconstruction of sand particles

Laser and structured light are two common scanning methods used for surface reconstruction of objects [7]. However, for sand particles, it is too small to be accurately captured by laser or structured light scanning methods. On

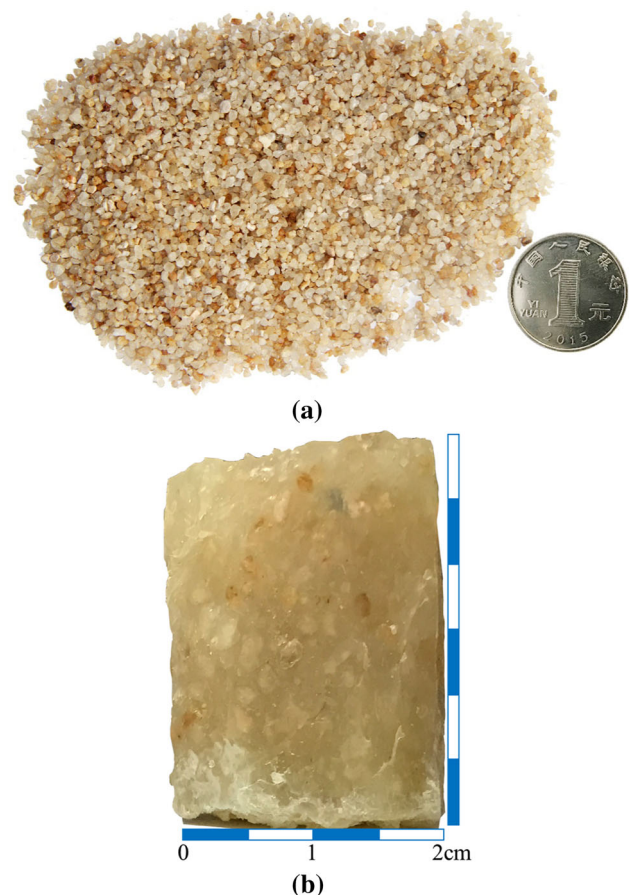


**Fig. 1** Sand particles used in this study: **a** sand particles; **b** sand sample mixed with silicone sealant

the other hand, CT has been widely used to obtain the internal structure of an object with high precision [10, 18]. Based on CT sequence images, the 3D fine geometric model of sand particles can be reconstructed.

To obtain an accurate contour of the sand particles through CT scan, it is ideal to keep the particles from being closely in contact. In this study, silicone sealant, which has a density much smaller than sand particles, is used to separate the particles. First, the sand particles were evenly mixed with the silicone sealant. The mixture was stirred enough to make sure that all the sand particles individually suspend in the silicone sealant. Then, the mixture was poured into a cylinder mold with lubricant. A cylinder mold with 2.0 cm in diameter and 3.0 cm in height was used. After the mixture solidified, the sample was taken out of the mold, and later used for CT scan (Fig. 1b).

To obtain the 3D CT sequence images of the sample, the Diondo D5 X-ray CT system is used (Fig. 2a). The rotation stage of Diondo D5 has a micro-step resolution of  $0.00^\circ$  and an absolute positioning accuracy of  $0.05^\circ$ . The detector consists of an image intensifier and a  $427 \text{ mm} \times 427 \text{ mm}$  CCD of  $3072 \times 3072$  pixels. During the scanning process, to obtain an effective source spot size of  $5 \text{ }\mu\text{m}$ , the voltage and current were held at 25 kV and 100  $\mu\text{A}$ , respectively. Under this condition, the resolution of the scanning is about 0.015 mm.

Based on the CT sequence images of the sand sample, its 3D model was reconstructed by using a software developed by Zhang et al. [38]. Note that it was easy to distinguish the individual particles through image separation since the particles were not closely in contact by using the sample preparation method described earlier. Figure 2b shows the schematic diagrams of 3D reconstruction process of the sand particles. Each of the 3D geometrical model of the sand particles was well captured and reconstructed.

## 2.2 3D geometrical characteristics of sand particles

Size and shape information of particles can be utilized in many fields of science and engineering to characterize the mechanical properties of a granular material [1, 2]. Over the last few decades, several methods have been introduced to quantitatively characterize particle shapes. To study the 3D geometrical features of the sand particles, a quantitative analysis and visualization module for particles were developed based on an open-source library named Visualization Toolkit (VTK). VTK is a C++ class library for 3D computer graphics and image processing that provides powerful 3D geometrical functions for quantitative analysis of objects. The developed module was integrated into Particle<sup>3D</sup>.

Size is the basic form dimensions of particles, which includes three length values length  $L$ , width  $W$ , and thickness  $T$ , which describe the extension of the particles along three suitable perpendicular directions. Generally, the three length values of a particle are obtained through its minimum volume bounding box (MVBB), which can be directly calculated by using VTK (Fig. 3). The particle length distribution curves based on 3D geometrical analysis are shown in Fig. 4a. Notice that the lengths of the sand particles range from 1.0 to 3.4 mm.

The sample was also characterized by using the traditional sieve analysis, which showed that particle sizes are between 1.2 and 2.0 mm, as mentioned earlier. In sieve vibration tests, most particles fall with its principal axial perpendicular to the sieve, as shown in Fig. 4a. This means that the particle size obtained through sieve analysis is closer to its width rather than its length. From the histogram of the three length values of the particles (Fig. 4a), it can be observed that the particle size range determined from sieve analysis is consistent with the width distribution that comes from the 3D geometrical analysis. Compared with simple sieve analysis, 3D geometrical analysis on sand samples can give more accurate measurements of particles in all three dimensions.

To categorize particle shapes, Zingg and Theodor [42] introduced a classification system according to the elongation  $W/L$  and flatness  $T/W$  of particles. This system is modified to incorporate four classes of particles, which are granules, chips, laths, and fibers. The classification analysis result of the sand sample used in this study is shown in Fig. 4b, which indicates that most of the particles are granules.

Figure 4c shows the relationship between surface area and volume of the sand particles. The particles are compared with three commonly used geometrical shapes: sphere, dodecahedron, and octahedron. The following exponential function describes a curve that is used to fit the statistical results:

$$SA = 5.8 V^{2/3}, \quad (1)$$

where  $SA$  and  $V$  are the surface area and volume of the particle, respectively. According to the relationship between surface area and volume, the sand particles are mostly close to octahedron.

Other than size and classification, several shape descriptors were used to provide more information on the geometrical features of the sand particles. The sphericity  $\psi$  and surface ratio  $S_r$  of a particle are defined:

$$\psi = \frac{\pi^{1/3}(6V)^{2/3}}{AS}, \quad (2)$$

$$S_r = AS/V. \quad (3)$$

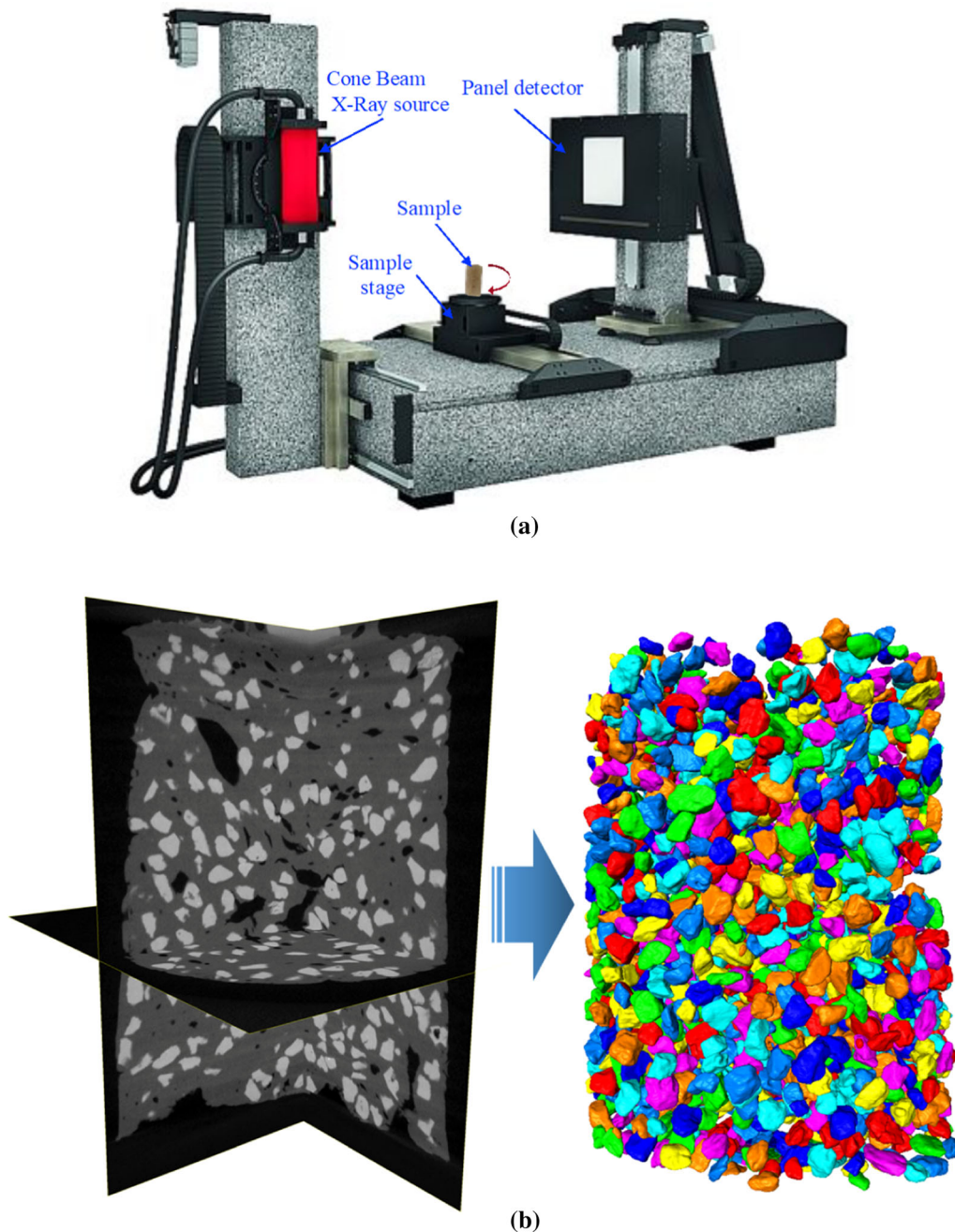


**Fig. 2** 3D reconstruction method of sand particles using CT system: **a** configuration of the Diondo D5 X-ray CT system; **b** 3D reconstruction of sand particles

Figure 5 shows the correlation between the two shape descriptors and particle length. As shown in Fig. 5a, the particle's sphericity decreases as the particle length increases. A linear function with negative slope can be used to describe the relationship between sphericity and particle length, which indicates that the smaller particles are more spherical. Figure 5b shows that the smaller particles have greater surface ratios. A power function, with an

exponent of  $-1$ , can be used to describe the relationship between the surface ratio and particle length.

Using the 3D numerical model of the sand specimen that was reconstructed from CT sequence images, the geometrical features of the sample particles were quantitatively analyzed. Compared with traditional analysis methods, the presented methodology can provide more accurate information on the particle sizes and shapes. According to the above statistical analysis results, the sand particles used in

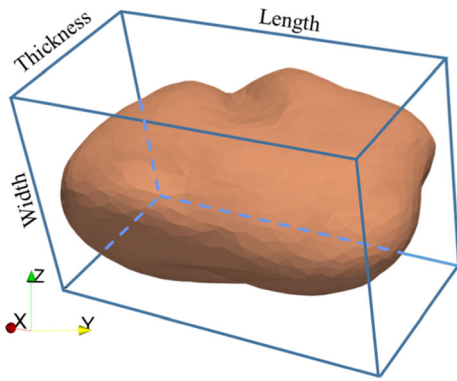


**Fig. 3** Size of a sand particle and its minimum volume bounding box (MVBB)

this study show strong regularity with respect to their geometrical attributes. Therefore, it is reasonable to use these particle models as a database to randomly generate a DEM model for the sand sample that is used in the following sections of this study.

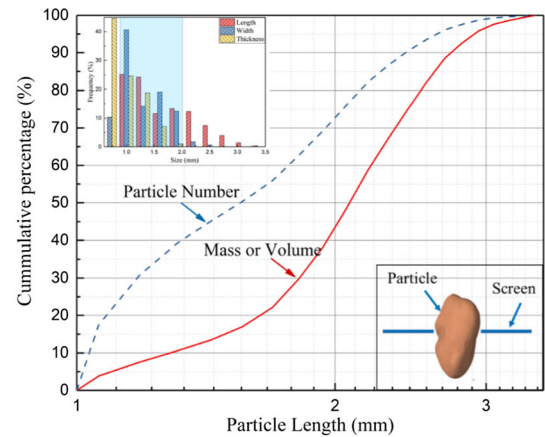
### 3 DEM simulations of direct shear tests

To investigate the macro- and meso-mechanical behaviors of sands, a series of DEM simulations of direct shear test were performed and analyzed. Using the approach described in the previous section, a proper DEM numerical model of the sand sample is generated. It is known that DEM simulation results are largely influenced by the contact properties between particles, which are hard to be determined directly. In this study, the meso-mechanical parameters were determined by calibrating the stress–displacement and dilatancy responses from the DEM simulations to those from corresponding laboratory tests.

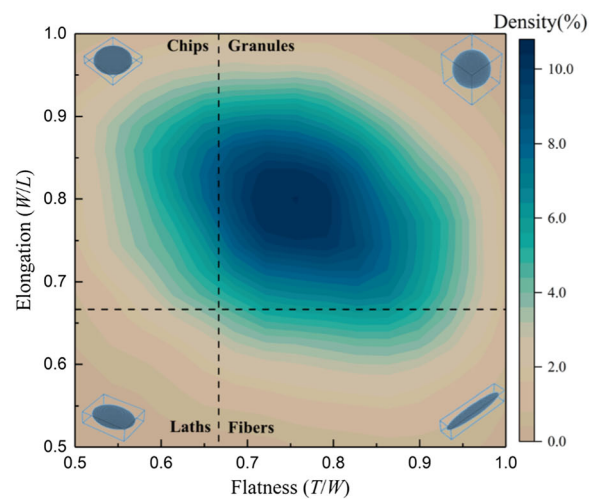
The DEM simulations in this study were conducted using YADE [14, 15], an open-source program based on 3D DEM. YADE uses an explicit finite difference algorithm, in which particle velocities and accelerations are assumed to be constant during each time step. The dynamic behavior of each particle is governed by Newton’s second law of motion, and the force at each contact is updated by force–displacement law. Numerical damping is applied to the system to achieve numerical stability, as well as a rapid convergence to equilibrium.

#### 3.1 DEM model generation and simulation process

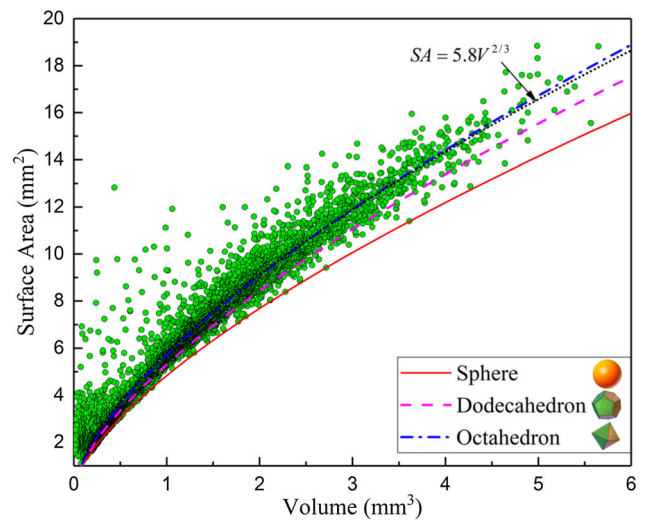
The geometrical models of the sand particles were selected randomly from the previously introduced 3D particle database. To represent the realistic shapes in DEM



(a)



(b)



(c)

**Fig. 4** Form dimensions of the sand particles: **a** particle length distribution curves; **b** classification of sand particle shape based on Zingg diagram; **c** relationship between surface area and volume

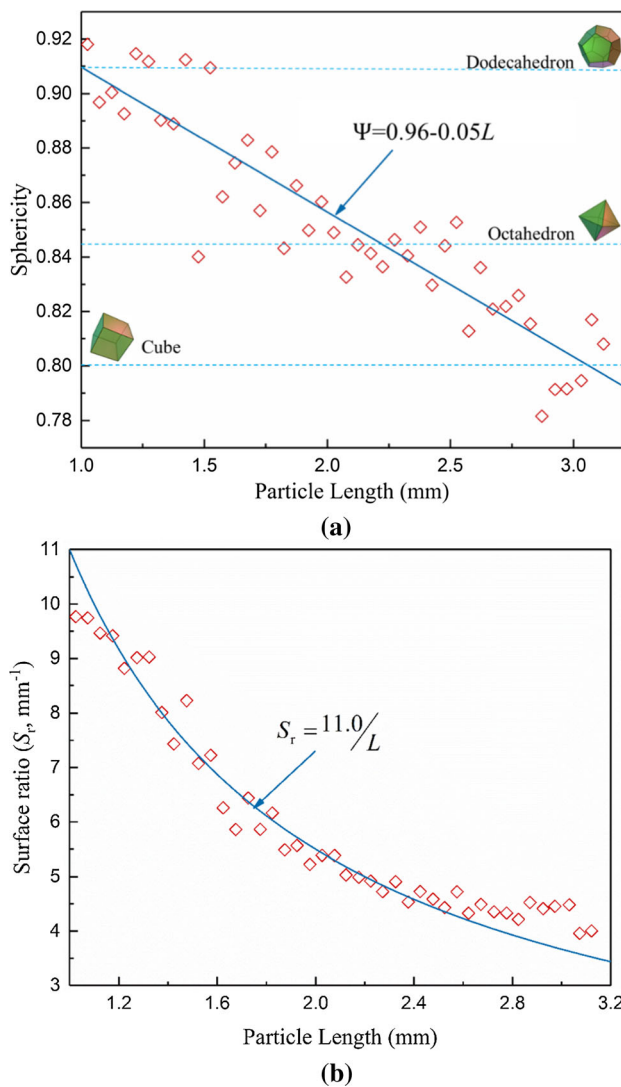


**Fig. 5** Shape descriptors of the sand particles: **a** relationship between the sphericity and particle length; **b** relationship between the surface ratio and particle length

simulation, the overlapping rigid cluster method [19] was used to generate the corresponding multi-sphere clumps.

As an example, the multi-sphere clump of a sand particle is shown in Fig. 6, which indicates that the clump can accurately describe the geometry of the sand particle with a small number of spheres.

The generated sand particles were dropped into a  $6.4 \text{ cm} \times 3.2 \text{ cm} \times 2.5 \text{ cm}$  box under gravity. Note that the particles were pluviated in several layers to ensure good compaction. Next, the samples were consolidated to equilibrium under a specified vertical stress, which was 50 kPa in this study. Then, the particles out of the sample range, a  $6.4 \text{ cm} \times 3.2 \text{ cm} \times 2.2 \text{ cm}$  rectangular space, were deleted. As shown in Fig. 7a, a final sample with 15,942 sand particles (multi-sphere clumps) and 430,822 spheres was generated and ready to be used for direct shear tests.

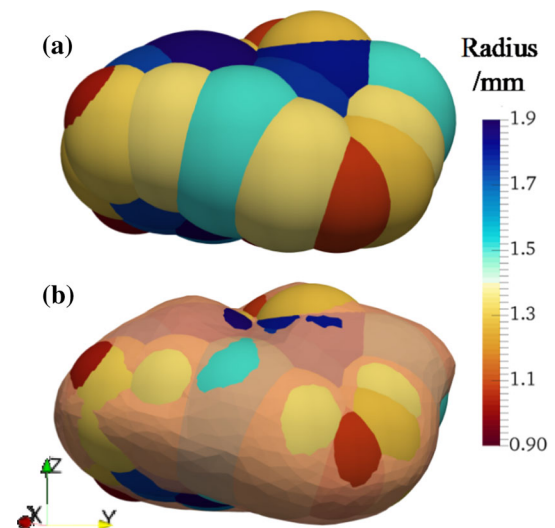


**Fig. 6** Multi-sphere description of the sand particle: **a** multi-sphere clump model; **b** comparison between the multi-sphere clump model and the corresponding particle model

The DEM model for the direct shear tests is shown in Fig. 7b. The upper and lower shear boxes were each made of five wall elements. The normal stress was applied to the top wall of the upper shear box using a servo-control mechanism that controls the velocity of the top wall so that the reaction force on the top wall reaches the target stress values and keeps stable. Then, the upper and lower shear boxes started to move with a constant velocity of  $6 \times 10^{-5} \text{ m/s}$  in the positive and negative directions of the  $x$ -axis, respectively, until the horizontal strain reaches 8%. Note that the normal stress was maintained at the target value with a relative tolerance of  $10^{-5}$  for the entire horizontal loading process.

During the simulations, the horizontal displacement, vertical displacement, and horizontal stress were recorded automatically. The movement of each particles and the development of the contact characteristics between particles were also recorded for further analysis that is presented in later sections.

### 3.2 Inversing meso-mechanical parameters based on laboratory tests

To determine the meso-mechanical parameters of the sand particles used in DEM simulation, a series of direct shear tests were performed in laboratory. The sand sample was sieved through a round-hole sieve to select the particles with size between 1.0 and 2.0 mm, which is the same range as that of the reconstructed 3D numerical models. The diameter and height of the shear box were 63.84 mm and 20 mm, respectively. The density of the compacted sample was  $1.58 \text{ g/cm}^3$ . And four laboratory tests under different

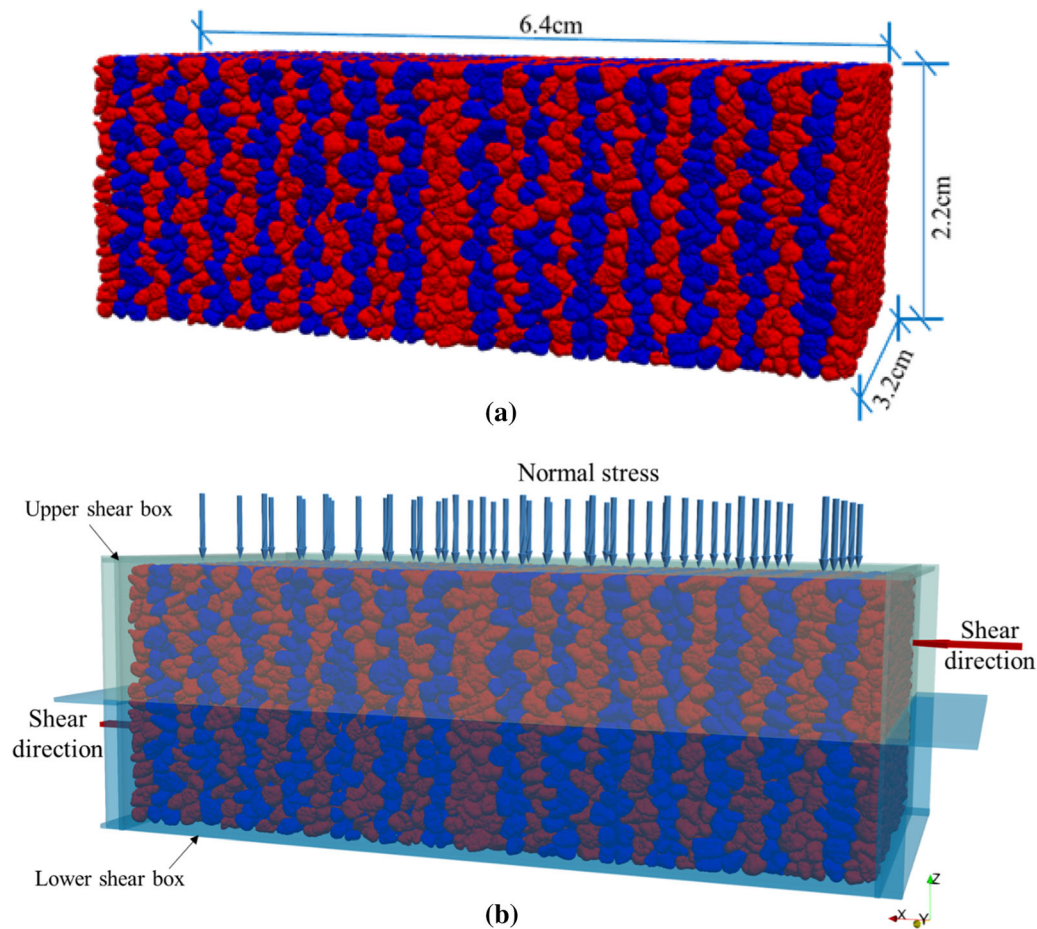


**Fig. 7** DEM model of the direct shear test (the color shows the horizontal position of the particle): **a** sand sample; **b** direct shear test

normal stress (100 kPa, 200 kPa, 300 kPa, and 400 kPa) were performed. As we know, particle breakage will happen during the shear process under higher stress state [31, 33]. To study the breakage characteristics, particles' size analysis before and after the shear tests has been performed for each sample, which showed that only very few particles broken during the tests. So, rigid particle and the friction contact model are used in DEM numerical tests.

The simulation results of the case with 200 kPa normal stress were benchmarked against the corresponding laboratory test results. For the friction contact model, the elastic modulus of contact and the friction angle of particles are the two important parameters. The former will influence the stiffness of the sample, and the latter will influence the strength of the sand sample on macro-scale, respectively. The meso-mechanical parameters of the sand particles were adjusted so that the shear stress–shear displacement and volumetric strain–shear displacement curves from the DEM simulation matched well with those from the laboratory test. Table 1 shows the meso-mechanical parameters of sand particles used in the DEM simulations.

To verify the reliability of the meso-mechanical parameters shown in Table 1, numerical and laboratory tests under other values of normal stress (100 kPa, 300 kPa, and 400 kPa) were conducted and analyzed. Figure 8 shows the comparison between the results of laboratory tests and DEM numerical tests. It can be observed that the results of all four cases corresponded well with each other. Therefore, the parameters shown in Table 1 can be used to represent the meso-mechanical properties of the sand particles in DEM simulations.

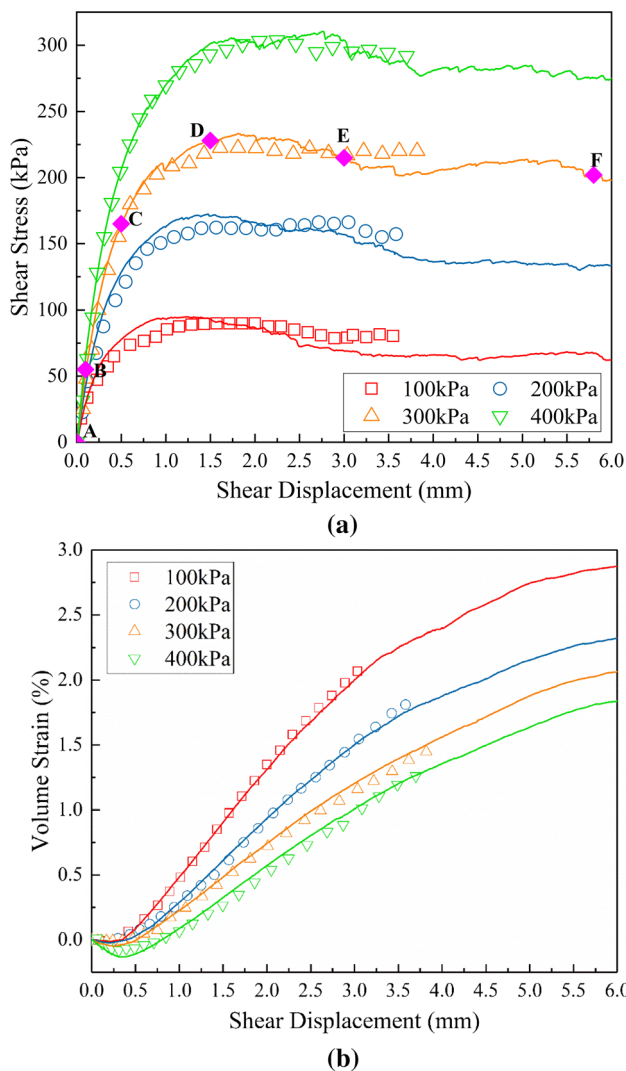
## 4 Numerical results analysis

### 4.1 Macro-mechanical behaviors

The shear stress–shear displacement curves, as shown in Fig. 8a, remained almost linear during the elastic loading stage (from point A to C). For all four cases with different normal stresses, strain softening occurred after the peak strength (point D), and the shear stresses reached stable values toward the end of simulations (from point E

**Table 1** Meso-mechanical parameters of materials used in DEM test

| Material      | Parameters   |      |
|---------------|--|------|
| Sand particle | Density ( $\text{kg/m}^3$ )  | 2100 |
|               | Elastic modulus of contact, $E_c$ (GPa)                              | 5    |
|               | Poisson's ratio of contact, $\nu$                                    | 0.1  |
|               | Friction angle ( $^\circ$ )  | 27.0 |
| Shear box     | Density ( $\text{kg/m}^3$ )  | 1000 |
|               | Elastic modulus of contact, $E_c$ (GPa)                              | 10   |
|               | Poisson's ratio of contact, $\nu$                                    | 0.1  |
|               | Friction angle between particle and top/bottom boundary ( $^\circ$ ) | 30.0 |
|               | Friction angle between particle and side boundary ( $^\circ$ )       | 0    |

**Fig. 8** Comparison between the results of laboratory tests (hollow points) and DEM numerical tests (solid lines): **a** shear stress–shear displacement; **b** volume strain–shear displacement

to F). It was also observed that the peak stresses were obtained at smaller displacements for the cases with smaller normal stresses.

From the volumetric strain–shear displacement curves (Fig. 8b), obvious bulk shrinkage was seen at the beginning of the test, which is an indication of typical loose sand. Then, the samples started to dilate as the shear stress–shear displacement curves became nonlinear. After the peak strength was reached, the rate of volume changes gradually decreased to almost zero. Also, the dilatancy of the DEM sample increased when the normal stress was decreased.

The results of the DEM tests corresponded well with those of the laboratory tests, which indicates that the generated numerical sample based on the real particle shapes can simulate the mechanical behaviors of the corresponding sand sample with a high accuracy, while, on the other hand, Salazar et al. [28] showed that DEM samples based on oversimplified spherical particles failed to accurately simulate the mechanical behaviors of sands during the plastic deformation stage when the volumetric strain is largely controlled by the shapes of particles.

## 4.2 Evolution of force chain distribution

For granular materials, the applied external force is balanced by the contact forces between particles throughout the entire sample. Such contact force network is usually known as the force chains, which is often used to describe the evolution of internal structure (or mesoscopic fabric) of particle assemblies. In this study, a statistical analysis zone was selected in the middle of the numerical sample, as shown in Fig. 9, to quantitatively analyze the evolution of force chains.

Figure 10 shows the evolution of some statistical parameters of the sand particles in the statistical zone for the case with 300 kPa normal stress.  $\bar{F}_n$  is the average value of the contact forces;  $P_{\text{strong}}$  and  $P_{\text{weak}}$  are the proportions of the strong and weak contacts, which are defined



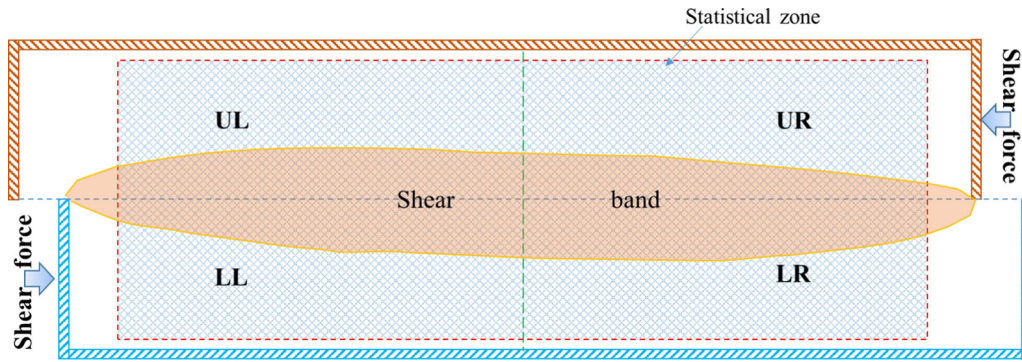


Fig. 9 Schematic diagram of the statistical zone and the sub-zones

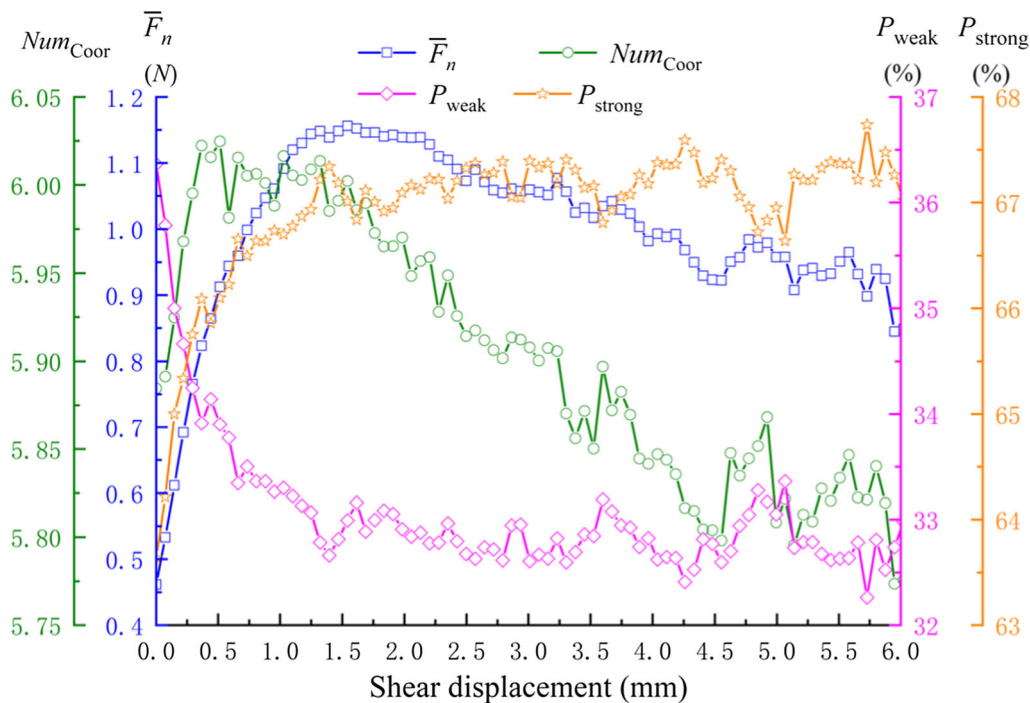


Fig. 10 Evolution of the contact characteristics of the sample (normal stress = 300 kPa)

as the contact with normal contact force larger or smaller than  $\bar{F}_n$ , respectively. The coordination number ( $Num_{Coor}$ ) is the average number of contacts per sand particle:

$$Num_{Coor} = 2N_c/N_p, \tag{4}$$

where  $N_c$  and  $N_p$  are the numbers of contacts and sand particles, respectively.

From Fig. 10, it can be seen that  $Num_{Coor}$  increased quickly during the beginning stage (point A to C in Fig. 8a) of the shearing test, which corresponds to the bulk shrinkage process of the sample at the macroscopic scale. The increase in  $Num_{Coor}$  means that more particles started to bear the external shear load, which leads to the sharp increase in shear stress observed in Fig. 8a. Then, from stage C to D, the deformation of the sample turned from mostly elastic to elastoplastic, and the volume of the

sample increased continuously. However,  $Num_{Coor}$  showed little change during this stage, which indicates that the evolution of the sample’s internal structure was mainly through the sliding between adjacent particles. After point D, the deformation of the sample turned to a strain softening stage along with the volumetric dilation, while the parameter  $Num_{Coor}$  kept decreasing gradually. This process continued until the shear displacement reached 4.5 mm when the values of the sample volume and  $Num_{Coor}$  became stable. Note that the value of  $Num_{Coor}$  was larger in this study than those reported in publication (less than 4.5 according to Guo and Zhao [9], Kruyt and Rothenburg [16] where simple spherical particles were used.

The evolutions of  $\bar{F}_n$  and  $P_{strong}$  were similar to those of the shear stress at the macroscopic scale. From A to C,  $\bar{F}_n$

and  $P_{\text{strong}}$  increase sharply, which corresponds to the increase in shear stress. Then, after the peak strength was obtained (point D),  $\bar{F}_n$  started to decrease slowly until the shear displacement reached 4.5 mm, while  $P_{\text{strong}}$  kept fluctuating within a stable range. Different from  $P_{\text{strong}}$ ,  $P_{\text{weak}}$  was observed to decrease sharply from A to D and then became stable during the strain softening stage.

Figure 11 shows the force chains of the sample under 300 kPa normal stress at different stages of shear loading, in which the colors and line widths represent the magnitudes of corresponding normal contact forces. According to Fig. 11a, after the consolidation stage (point A), the strong force chain distribution was heterogeneous and anisotropic with a principal direction in the vertical direction. Note that such heterogeneity and anisotropy can often be observed in various natural deposits. By using particle models with realistic shapes, the DEM simulations presented in this study can capture these characteristics of granular materials and thus yield more realistic simulations results.

As shown in Fig. 11b, from stage A to B, the shear displacement only increased by 0.1 mm (about 0.15% shear strain), but the structure of the force chains evolved drastically. The force chains, especially those with large contact forces, mainly distributed in a banding zone from the upper right to the lower left part of the sample. During the bulk shrinkage stage, from stage A to C, the number of the strong force chains was observed to increase significantly, which is consistent with the plot of  $P_{\text{strong}}$  shown in Fig. 10. Then, as the shear displacement increased from C

to E, the region of strong force chains became more narrow and stable. A skeleton composed of a series of parallel strong force chain arches, which connect the upper right to the lower left boundaries of the sample, was formed. From E to F, during the strain softening stage, the penetrating force chains were being destroyed by the large shear displacement, which explains the drop of external shear load.

During the deformation and failure process of granular material under external loads, the mesoscopic fabric of the sample continues to evolve. This evolution of internal structure comes from the rotation and displacement of particles, as well as the corresponding adjustments of the contact characteristics between particles such as coordinate number, contact forces, and contact direction. As observed in the plots of force chains (Fig. 11), the fabric evolution in granular material is always anisotropic, which is another important aspect of the mesoscopic analysis of DEM simulation results.

### 4.3 Evolution of stress-induced anisotropy

Stress-induced anisotropy, defined as the anisotropic rearrangement of particles during external loading [4], is considered to have a significant influence on the mechanical behavior of granular material. Evidence of stress-induced anisotropy was observed in the evolution of the force chains shown in Fig. 11. The quantitative analysis of the evolution of anisotropy was performed using the spherical harmonic series method presented by Yang et al. [36].

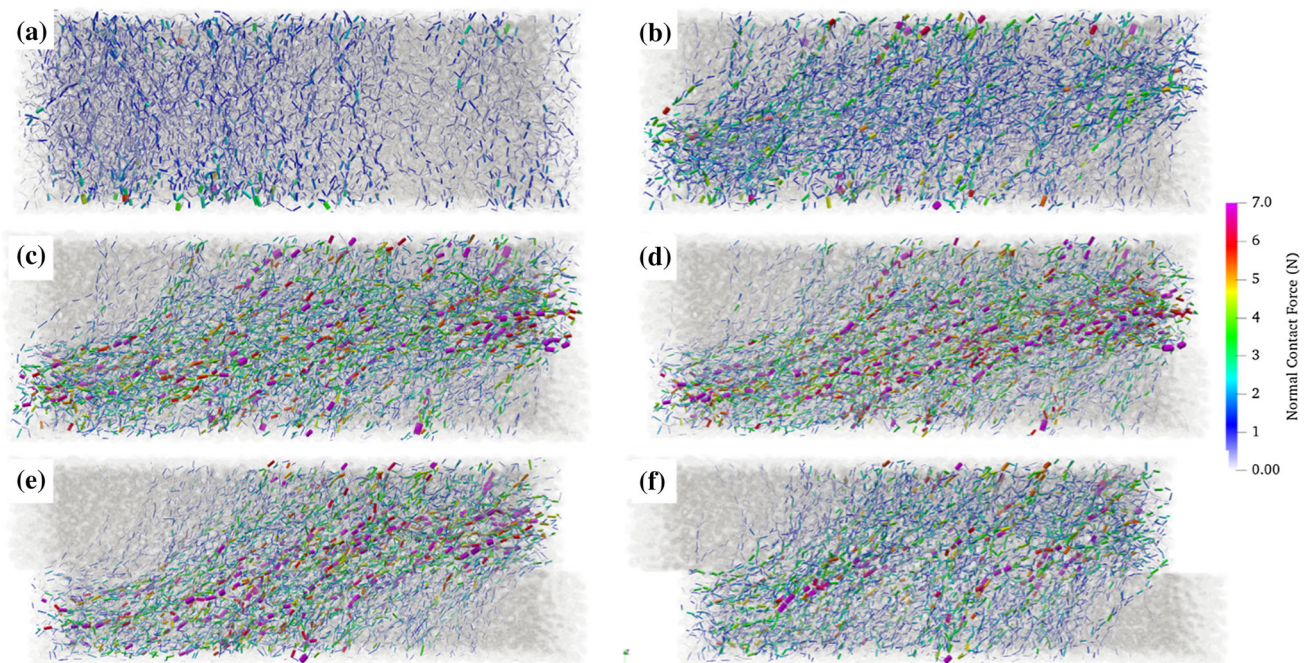


**Fig. 11** Force chains of the sample (normal stress = 300 kPa) at a different shearing process as shown in Fig. 8a: **a** Point A; **b** Point B; **c** Point C; **d** Point D; **e** Point E; **f** Point F

The general digital modeling expression of irregular geometrical bodies in spherical coordinate system, given by Luerkens [21], is modified by Yang et al. [36] to describe the anisotropic statistical results of the DEM direct shear simulations:

$$R_f(\theta, \phi) = \alpha_{00} + \alpha_{20} \cdot \frac{1}{2}(3 \cos^2 \theta - 1) + \alpha_{22} \cos 2\phi \cdot 3 \sin^2 \theta + \alpha_{40} \cdot \frac{1}{8}(35 \cos^4 \theta - 30 \cos^2 \theta + 3), \tag{5}$$

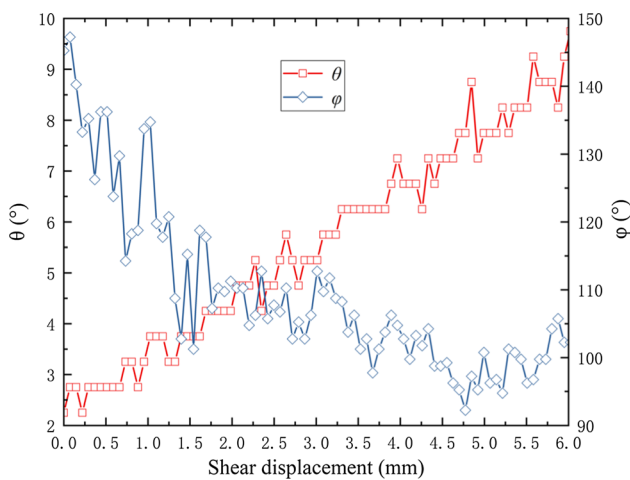
where  $\theta$  is the angle between the anisotropy principal direction and horizontal plane;  $\phi$  is the angle between the projection of the anisotropy principal direction on the horizontal plane and the direction of shear displacement;  $R_f(\theta, \phi)$  is the value of the statistical parameter (normalized contact number, normal contact force, or tangential contact force) in the direction defined by  $\theta$  and  $\phi$ ;  $\alpha_{nm}$  and  $\beta_{nm}$  are the Fourier–Legendre coefficients used to represent

the level of anisotropy, which are given by: where  $P_n^m(\cos \theta)$  is the associated Legendre function.

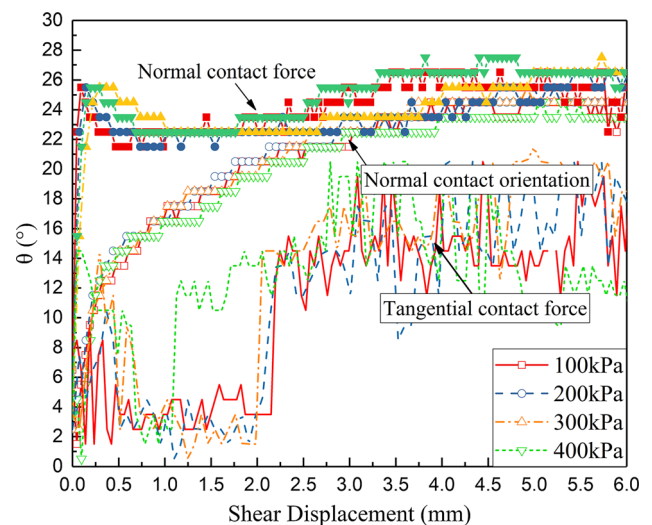
Figure 12 shows the evolution of the principal axes of the particles. Initially, the value of  $\theta$  was about  $2.5^\circ$  which means that most of the particles had principal directions that are close to the horizontal plane. This inherent anisotropy was formed during the pluviation of particles with realistic shapes under gravity. As the shear displacement increased, the value of  $\theta$  continued to increase to about  $10^\circ$ . Meanwhile, the value of  $\phi$  fluctuated and stabilized at around  $90^\circ$ , which is perpendicular to the direction of shear loading.

Figure 13 shows the evolution of the anisotropy principal directions of the contact direction, normal contact force, and tangential contact force during the shearing process. Compared to the numerical results shown in a study using simplified spherical particles by Yang et al. [36], the anisotropy analysis results obtained in this study showed some similarities in terms of the overall trend of

$$\begin{cases} \alpha_{m,n} = \frac{(2n+1)(n-m)!}{2\pi(n+m)!} \int_{-1}^1 \int_0^{2\pi} R(\theta, \phi) P_n^m(\cos \theta) \cos(m\theta) d\theta d \cos \theta \\ \beta_{m,n} = \frac{(2n+1)(n-m)!}{2\pi(n+m)!} \int_{-1}^1 \int_0^{2\pi} R(\theta, \phi) P_n^m(\cos \theta) \sin(m\theta) d\theta d \cos \theta \end{cases}, \tag{6}$$



**Fig. 12** Evolution of the anisotropy direction of the particle’s principal axis during the shear tests ( $\theta$  is the angle between the anisotropy principal direction and horizontal plane;  $\phi$  is the angle between the projection of the anisotropy principal direction on the horizontal plane and the  $x$ -axis or shear direction)



**Fig. 13** Evolution of the anisotropy principal direction of the contact characteristics during the shear tests ( $\theta_n$  is the angle of the anisotropy principal direction of the contact normal orientation with the horizontal direction, while  $\theta_n$  and  $\theta_t$  are the angle of the anisotropy principal direction of normal contact force and tangential contact force with vertical direction, respectively)

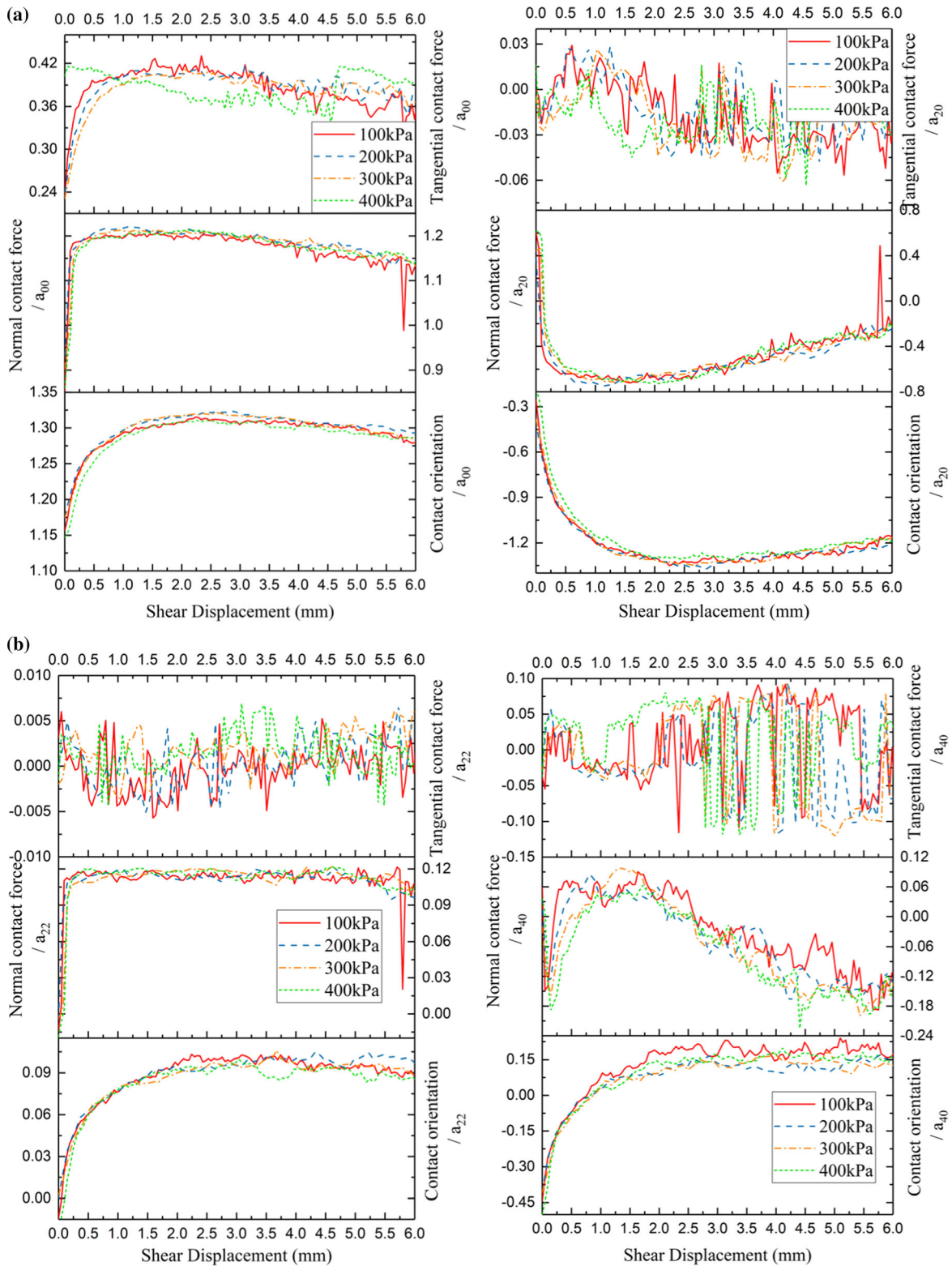


**Fig. 14** Evolution of anisotropy parameters of sample under a different vertical stress during the shear tests: **a**  $a_{00}$ ; **b**  $a_{20}$ ; **c**  $a_{22}$ ; **d**  $a_{40}$ ; **e**  $b_{22}$

evolution of the anisotropy parameters and principal directions. However, due to the use of realistically shaped particles, the translational and rotational movements of the

particles were more sudden and violent, which lead to stronger fluctuations in the evolution of stress-induced anisotropy in the sample. Also, it was observed that the

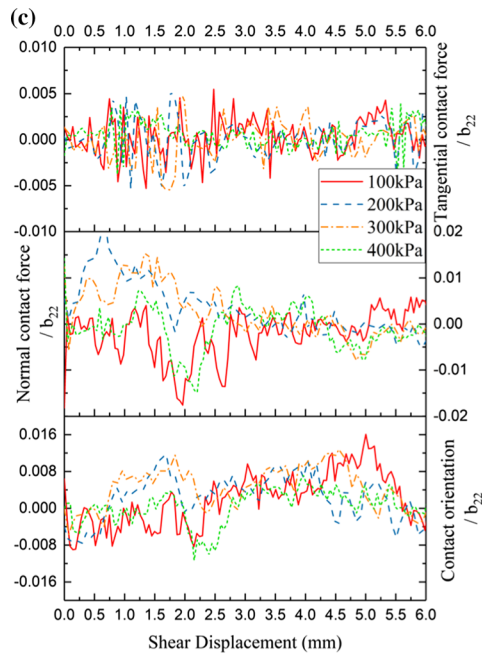


Fig. 14 continued

anisotropy of the normal contact force is stronger than of the contact normal orientation in this study, while it was the opposite for spherical particles as reported by Yang et al. [36].

A good correspondence between the curve of anisotropy principal direction of the contact normal orientation  $\theta_n$  in Fig. 13 and the development of shear stress in Fig. 8a was observed in all four cases. At the initial state,  $\theta_n$  is about  $2^\circ$  which means that most of the contacts were nearly in the horizontal direction. This result is consistent with the initial principal directions of the particles shown in Fig. 12. As the shearing progressed, the principal direction of the contacts rotated counterclockwise and reached a stable value of about  $26^\circ$  with the horizontal plane.

The evolution of the principal direction of the normal contact force  $\theta_a$  is different than that of  $\theta_n$ , which indicates that most of the external loads were carried by a small number of particles. Before the shearing started, because of the normal stress, the principal direction of the normal contact force was very close to the vertical direction. After the shear displacement was applied,  $\theta_a$  quickly increased to about  $26^\circ$ , which is the same as the stable value of  $\theta_n$ . Note that a peak in the curve of  $\theta_a$  was observed at the shear displacement where the maximum bulk shrinkage occurred.

The development of the principal direction of the tangential contact force  $\theta_t$  was slower than those of the other two principal directions ( $\theta_n$  and  $\theta_a$ ). In this study,  $\theta_t$  fluctuated sharply during the whole shearing process, which is likely due to the sudden relative sliding between the

realistically shaped particles. Also, from the evolution of  $\theta_t$  shown in Fig. 13, the sliding displacement mostly happened after the peak shear stress was reached (point D in Fig. 8a).

Figure 14 shows the evolution of the Fourier–Legendre coefficients used to represent the level of anisotropy of sample under different normal stresses during the shear tests. For the tangential contact force, just as the corresponding principal direction  $\theta_t$ , the evolution of the Fourier–Legendre coefficients also had sharp fluctuations, but the overall changes of their values were insignificant. Because the realistic shapes of the particles were highly irregular, the rotational and translational movements of the particles were largely controlled by the normal contact forces rather than the tangential contact forces. On the other hand, if simplified spherical shapes were used for the particles, their rotations would be controlled by the tangential contact forces.

For the normal contact orientation and the normal contact force, the evolutions of their Fourier–Legendre coefficients were similar to each other. The anisotropy parameters evolved quickly during the beginning stage of the shearing process and then became stable after the peak shear stress was reached. Like the comparison between the anisotropy principal directions  $\theta_n$  and  $\theta_a$ , the evolutions of the normal contact force parameters were quicker than those of the normal contact orientation.

#### 4.4 Deformation localization analysis

To obtain the deformation characteristics of the sample, Voronoi diagram was generated based on the center and radius of the spheres in the multi-sphere clumps used to model the sand particles. As shown in Fig. 15, the Voronoi cell corresponding to each sphere can be obtained, and then, the volume of each multi-sphere clump (or sand particle) can be calculated:

$$V_p^i = \sum_{j=1}^m V_{\text{Vor}}^{i,j}, \quad (7)$$

where  $V_p^i$  is the volume of the  $i$ th multi-sphere clump, which includes the volume of the solid particle and the volume of the influenced pore;  $V_{\text{Vor}}^{i,j}$  is the volume of the Voronoi cell corresponding to the  $j$ th sphere in the  $i$ th multi-sphere clump;  $m$  is the total number of spheres in the  $i$ th clump.

The volumetric strain of each multi-sphere clump is defined as:

$$\varepsilon_v^i(t) = \frac{V_p^i(t) - V_p^i(0)}{V_p^i(0)} \cdot 100\%, \quad (8)$$

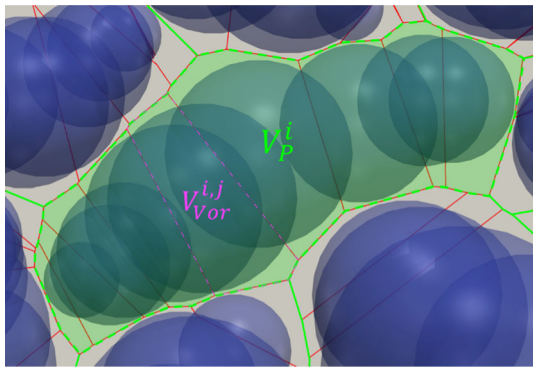


**Fig. 15** Schematic diagram of the particle clump's volume based on Voronoi cell

where  $\varepsilon_v^i(t)$  is volumetric strain of the  $i$ th clump at time  $t$ ,  $V_p^i(t)$  is volume of the  $i$ th clump at time  $t$ , and  $V_p^i(0)$  is volume of the  $i$ th clump at the beginning of the shearing process. Since the volume of the solid particles is constant, the change of the particle clump volume is caused by the evolution of shapes of the surrounding pores. Therefore,  $\varepsilon_v^i(t)$  can be used to describe the change of the pores' volume, which is a key factor in the deformation location of granular material.

Figure 16 shows the evolution of the displacements, rotations, and volumetric strains of the multi-sphere particles. At the beginning of the shearing process (point A to C), the particles near the shear surface were in compression ( $\varepsilon_v^i(t) < 0$ ). Due to stress concentration, localization started

to develop from the two ends of the shear surface. According to the relative movement of the shear boxes, the sample was divided into an active zone (UL, LR) and a passive zone (UR, LL), as shown in Fig. 9. The particles in the passive zone were tightly constrained by the adjacent particles, which made their rotations more difficult than those of the particles in the active zone where the contact forces were weaker. Therefore, the localization behavior was first triggered in the active zone, and the initial shear band had the shape of an asymmetric lens.

With the development of shear displacement, particle movements and rotations caused the pore volume to increase near the shear surface (Fig. 16b, c), which slowed down the rate of increase in the shear stress. Then, the localization zone was observed to penetrate the entire shear surface and stabilized, which corresponds with the strain softening stage of the sample (Fig. 16d, e). Due to the random realistic shapes of the particles, the distribution of volume strain in the localization zone was highly inconsistent. From Fig. 16, it was observed that the thickness of the localization zone is about 10 particle sizes.

## 5 Conclusions

Fabric evolution of granular material under external loads is a critical issue in geomechanics. Taking advantage of the CT technique and DEM, numerical simulations have been performed to investigate the geometrical characteristics of

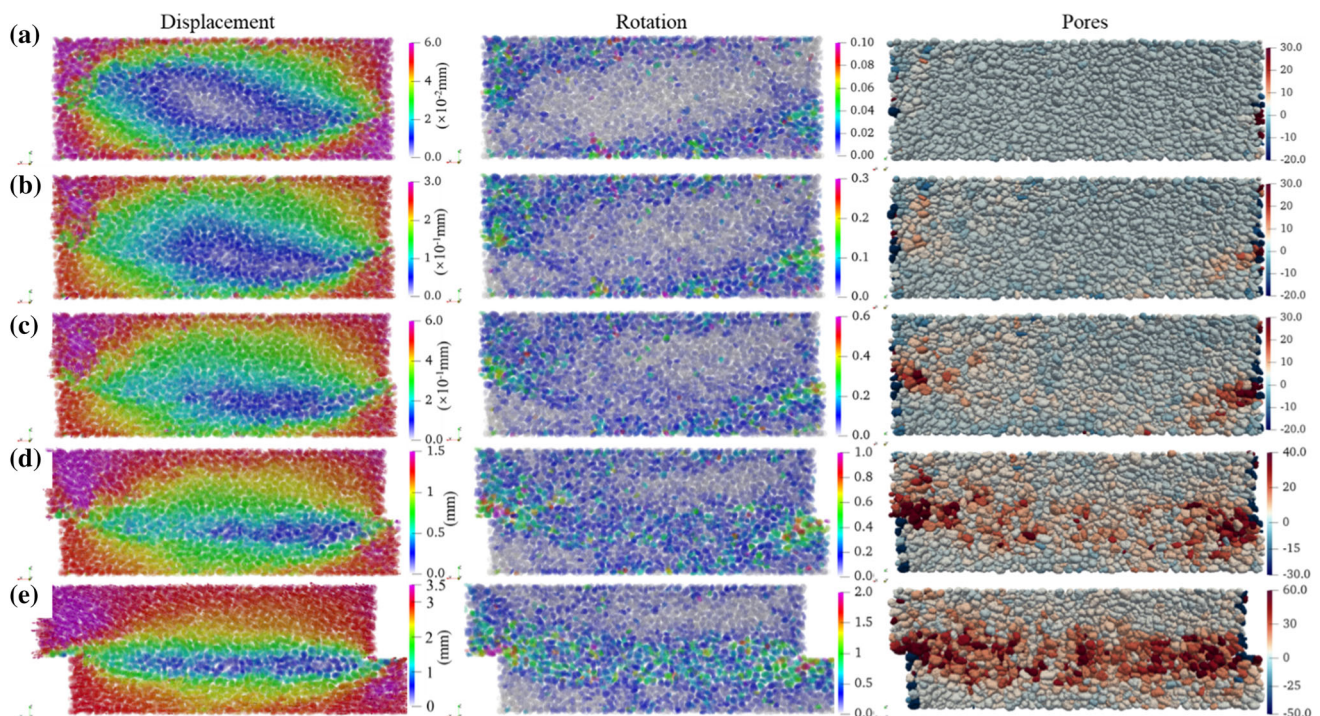


**Fig. 16** Evolution of the localization of deformation: **a** Point B; **b** Point C; **c** Point D; **d** Point E; **e** Point F

sand particles and the mechanical behavior of granular material under direct shear loading. Macroscopic and mesoscopic analysis based on the simulation results has been conducted to give insights on the evolution of heterogeneity and anisotropy in the localized shear zones in sand samples.

A reconstruction method of granular particles has been presented and used to build a database of 3D geometrical models for sand particles. A quantitative analysis indicated that the particle sizes determined from the traditional sieve analysis are close to the actual widths, rather than the lengths, of the sand particles. The studied sand particles showed good regularities in morphological characteristics and thus were suitable to be used for the random generation of numerical samples.

The DEM results corresponded well with those of the laboratory tests, which were used to calibrate the meso-mechanical parameters. DEM tests using realistically shaped particles were proven to better simulate the mechanical behavior of the sample during elastoplastic loading stage, which was an issue for the simplified spherical particles.

The mechanical behavior of the sample was largely controlled by the strong force chains, which were observed to have formed before the peak stress was reached. The breakage, extension, and generation of force chain arches happened post-peak stress and lead to strain softening. The complex geometry of the particles also increased the value of the coordination number.

Anisotropy analysis using the spherical harmonic series showed that the evolution of anisotropy directions and parameters corresponded well with the macroscopic mechanical behavior of the material. Compared to the previous studies using spherical shaped particles, realistically shaped particles better simulated the influences of normal and tangential contact forces toward the anisotropic evolution of the material fabric.

Pore volume computation based on Voronoi diagram was performed to analyze the formation of localized shear zone, which was critical to the overall mechanical behavior of the granular material. The plots of the displacements and rotations of the particles, as well as the pore volume, all showed that deformation localization occurred and evolved during the shearing process. The thickness of the localization zone was about 10 particle sizes.

**Acknowledgements** The authors would like to acknowledge the project of “The National Key Research and Development Program of China, China (2017YFC0805406),” “Natural Science Foundation of China (51679123, 51879142),” “Research Fund Program of the State Key Laboratory of Hydroscience and Engineering (2020-KY-04).”

## References

- Asahina D, Taylor MA (2011) Geometry of irregular particles: direct surface measurements by 3-D laser scanner. *Powder Technol* 213(1–3):70–78
- Bagheri GH, Bonadonna C, Manzella I, Vonlanthen P (2015) On the characterization of size and shape of irregular particles. *Powder Technol* 270:141–153
- Bagherzadeh-Khalkhali A, Mirghasemi AA (2009) Numerical and experimental direct shear tests for coarse-grained soils. *Particuology* 07(1):83–91
- Casagrande A, Carillo N (1944) Shear failure of anisotropic materials. *Proc Boston Soc Civ Eng* 31:74–87
- Charalampidou EM, Hall SA, Stanchits S, Lewis H, Viggiani G (2011) Characterization of shear and compaction bands in a porous sandstone deformed under triaxial compression. *Tectonophysics* 503(1–2):8–17
- Cho N, Martin CD, Sego DC (2008) Development of a shear zone in brittle rock subjected to direct shear. *Int J Rock Mech Min Sci* 45(8):1335–1346
- Feng ZK, Xu WJ, Lubbe R (2020) Three-dimensional morphological characteristics of particles in nature and its application for DEM simulation. *Powder Technol* 364:635–646
- Govender N, Wilke DN, Kok S (2015) Collision detection of convex polyhedra on the NVIDIA GPU architecture for the discrete element method. *Appl Math Comput* 267:810–829
- Guo N, Zhao J (2013) The signature of shear-induced anisotropy in granular media. *Comput Geotech* 47(1):1–15
- Gupta R, Salager S, Wang K et al (2019) Open-source support toward validating and falsifying discrete mechanics models using synthetic granular materials-Part I: experimental tests with particles manufactured by a 3D printer. *Acta Geotech* 14:923–937
- Hyslip JP, Vallejo LE (1997) Fractal analysis of the roughness and size distribution of granular materials. *Eng Geol* 48(3):231–244
- Iwashita K, Oda M (1998) Rolling resistance at contacts in simulation of shear band development by DEM. *J Eng Mech ASCE* 124:285–292
- Ishida T, Kanagawa T, Kanaori Y (2010) Source distribution of acoustic emissions during an in situ direct shear test: implications for an analog model of seismogenic faulting in an inhomogeneous rock mass. *Eng Geol* 110(3–4):66–76
- Kozicki J, Donzé FV (2008) A new open-source software developed for numerical simulations using discrete modeling methods. *Comput Methods Appl Mech Eng* 197(49):4429–4443
- Kozicki J, Donzé FV (2009) YADE-OPEN DEM: an open-source software using a discrete element method to simulate granular material. *Eng Comput* 26(7):786–805
- Kruyt NP, Rothenburg L (2016) A micromechanical study of dilatancy of granular materials. *J Mech Phys Solids* 95:411–427
- Kuhn MR (1999) Structured deformation in granular materials. *Mech Mater* 31(6):407–429
- Lai Z, Chen Q (2019) Reconstructing granular particles from X-ray computed tomography using the TWS machine learning tool and the level set method. *Acta Geotech* 14:1–18
- Li CQ, Xu WJ, Meng QS (2015) Multi-sphere approximation of real particles for DEM simulation based on a modified greedy heuristic algorithm. *Powder Technol* 286:478–487
- Lin X, Ng TT (1997) A three-dimensional discrete element model using arrays of ellipsoids. *Géotechnique* 47(2):319–329
- Luerkens D (1986) Particle surface morphologies—the three dimensional particle. *Part Sci Technol* 4(4):371–378
- Mollon G, Zhao J (2012) Fourier–Voronoi-based generation of realistic samples for discrete modelling of granular materials. *Granul Matter* 14(5):621–638

23. Oyanguren PR, Nicieza CG, Fernández MIÁ, Palacio CG (2008) Stability analysis of Llerin Rockfill Dam: an in situ direct shear test. *Eng Geol* 100(3):120–130
24. Peters JF, Hopkins MA, Kala R, Wahl RE (2009) A poly-ellipsoid particle for non-spherical discrete element method. *Eng Comput* 26(6):645–657
25. Rechenmacher AL, Abedi A, Chupin O (2010) Evolution of force chains in shear bands in sand. *Géotechnique* 60(5):343–351
26. Reid K, Edward A, Gioacchino V et al (2016) Level set discrete element method for three-dimensional computations with triaxial case study. *J Mech Phys Solids* 91:1–13
27. Rothenburg L, Bathurst RJ (1993) Influence of particle eccentricity on micromechanical behavior of granular materials. *Mech Mater* 16(1):141–152
28. Salazar A, Sáez E, Pardo G (2015) Modeling the direct shear test of a coarse sand using the 3D discrete element method with a rolling friction model. *Comput Geotech* 67:83–93
29. Santamarina JC, Cho GC (2004) Soil behaviour: the role of particle shape. *Proceedings of the skempton conference*, March, London
30. Thornton C (2000) Numerical simulations of deviatoric shear deformation of granular media. *Géotechnique* 47(2):319–329
31. Ueng TS, Chen TJ (2000) Energy aspects of particle breakage in drained shear of sands. *Geotechnique* 50(1):65–72
32. Wang J, Dove JE, Gutierrez MS (2007) Discrete-continuum analysis of shear banding in the direct shear test. *Géotechnique* 57(6):513–526
33. Xiao Y, Liu H, Desai CS, Sun Y, Liu H (2016) Effect of intermediate principal-stress ratio on particle breakage of rockfill material. *J Geotech Geoenviron Eng* 142(4):06015017
34. Xiao Y, Long L, Matthew Evans T et al (2019) Effect of particle shape on stress–dilatancy responses of medium-dense sands. *J Geotech Geoenviron Eng* 145(2):04018105
35. Xu WJ, Xu Q, Hu RL (2011) Study on the shear strength of soil–rock mixture by large scale direct shear test. *Int J Rock Mech Min Sci* 48(8):1235–1247
36. Yang H, Xu WJ, Sun QC, Feng Y (2017) Study on the meso-structure development in direct shear tests of a granular material. *Powder Technol* 314(1):129–139
37. Yang J, Wei LM (2012) Collapse of loose sand with the addition of fines: the role of particle shape. *Geotechnique* 62(12):1111–1125
38. Zhang HY, Xu WJ, Yu YZ (2016) Triaxial tests of soil–rock mixtures with different rock block distributions. *Soils Found* 56(1):44–56
39. Zhang L, Thornton C (2007) A numerical examination of the direct shear test. *Géotechnique* 57(4):343–354
40. Zhao SW, Zhou XW, Liu WH (2015) Discrete element simulations of direct shear tests with particle angularity effect. *Granul Matter* 17:793–806
41. Zhao SW, Evans TM, Zhou XW (2018) Shear-induced anisotropy of granular materials with rolling resistance and particle shape effects. *Int J Solids Struct* 150:268–281
42. Zingg & Theodor (1935) Beitrag zur schotteranalyse. *Mineral Petrol Mitt* 15:39–140

**Publisher's Note** Springer Nature remains neutral with regard to jurisdictional claims in published maps and institutional affiliations.